

Theoretical investigation of electric-field noise emanating from vibrational adatomsJiarui Zeng,¹ Xiao-Tong Yan,¹ Yao Yao ^{1,2,*} Yu-Jun Zhao,¹ Liang Chen,^{3,4,†} and Mang Feng ^{3,4,5,‡}¹*Department of Physics, South China University of Technology, Guangzhou 510640, China*²*State Key Laboratory of Luminescent Materials and Devices, South China University of Technology, Guangzhou 510640, China*³*State Key Laboratory of Magnetic Resonance and Atomic and Molecular Physics, Wuhan Institute of Physics and Mathematics, Innovation Academy of Precision Measurement Science and Technology, Chinese Academy of Sciences, Wuhan 430071, China*⁴*Research Center for Quantum Precision Measurement, Guangzhou Institute of Industry Technology, Guangzhou 511458, China*⁵*Department of Physics, Zhejiang Normal University, Jinhua 321004, China*

(Received 13 August 2022; accepted 11 August 2023; published 23 August 2023)

Electric-field noise stemming from surface adsorption of atoms serves as the main factor of anomalous motional heating and decoherence for trapped ions confined in harmonic potentials of surface-electrode traps. However, this also provides a possible way for ions playing as nanosensors to detect surface defects and explore the mechanism of noise. Taking monatomic vibrations on the surface into account, here we calculate the electric-field noise and discuss its spectral properties by utilizing density-functional theory and the incoherent master equation with fitting parameters. We find that most adatoms lead to universal spectral intensity and frequency scaling. Particularly, we discover a colored feature for the weak-binding Ar adatom with the increase of the temperature, which can be attributed to the anharmonic potential and high-lying vibrational states. Our results could be helpful for understanding the mechanism of the surface noise and developing efficient noise-detection methods.

DOI: [10.1103/PhysRevA.108.023121](https://doi.org/10.1103/PhysRevA.108.023121)**I. INTRODUCTION**

Trapped ions are considered to be one of the promising candidates for quantum computation and simulation due to high fidelities of the operations and excellent coherence of the qubits [1–3]. However, fluctuation of the electric fields, i.e., the electric-field noise, is the main detrimental factor leading to the anomalous heating and/or decoherence of the trapped ions [4,5]. Previous experimental studies have revealed a common distance-dependent behavior of the intensity of the noise spectrum, $S_E \sim d^{-4}$, implying that the noise would be the main challenge for the miniaturization of the ion traps [4]. In this context, the origin of the electric-field noise has been a major focus during the past several decades.

In general, the ambient noise in such systems is described by Johnson noise associated with thermally fluctuating dipole oscillators in the electrode bulk. But there exist other noises emerging from unknown sources, which are beyond the Johnson noise [6,7]. Recent experimental and theoretical studies have indicated that these unexpected noises might be from the adsorbates and dielectric materials on the electrode surface [8–16]. Some evidences have been demonstrated that the intensity of the electric-field noise can be significantly reduced after appropriate surface treatments [9]. Theoretical models of the adatom vibration and diffusion also predict a distance scaling consistent with the experimental results [4,12,14].

The mechanism of the electric-field noise is not yet comprehensively clarified. Particularly for real systems there might be multiple complicated mechanisms [17]. To understand the underlying mechanisms, it has been suggested to employ trapped ions as nanoprobe to detect the noises [9]. This is a different way of exploring the noise mechanisms, helpful for improving the performance of quantum computing using trapped ions and analyzing surfaces to complement the existing surface-science techniques. With such nanosensors, the general scalings of the spectral intensity with respect to the trap's secular frequency, the ion-surface separation, and the ion's temperature have been applied to distinguish the noise sources in realistic ion-trap systems [17–20]. Recent works have also pointed out the nontrivial influences from the species, coverage, and even thermal transformations of the adsorbates on the trap electrodes [21,22]. We have also noticed recent reports about noninvasive measurements of the superconducting transition, based on the possible surface noise [23,24].

Moreover, theoretical studies involving density-functional theory (DFT) have been developed extensively to approach realistic cases [12–14,25–29]. Taking into account the effect of surface patches, a surface diffusion model has obtained spectral intensity in good agreement with experimental results [14]. Combining DFT with the method of molecular dynamics, Foulon *et al.* [29] have considered interactive adsorbates and different coverages in investigating the emergence of $1/f$ frequency scaling. In another adatom model describing the vibration-induced fluctuating dipole moment, Ray *et al.* [27] have calculated the noise spectra for a range of adsorbed species in the discussion of their frequency and thermal

*yaoyao2016@scut.edu.cn

†liangchen@wipm.ac.cn

‡mangfeng@wipm.ac.cn

features. The results indicate that most of the adsorbates have a very narrow region with $1/f$ scaling. However, this scaling seems to appear in the high-frequency region if the phonon exchange mechanism of the adatoms is considered [28].

To provide comprehending understanding of the adsorbed systems, we perform numerical calculations in the present paper for the noise spectra of two kinds of adatoms with strong and weak binding, respectively, which are adsorbed on the Cu(100) surface and cause the fluctuation of the electric dipole moment via nuclear vibration. Different from the previous works, here we focus on the relationship between the high-lying vibrational states and low-frequency noise. Our results show that for the weak-binding Ar adatom, an anharmonic potential would lead to a colored feature in the low-frequency region, different from the conventional viewpoint of the white noise. This possibly provides a new origin of the colored noise due to many mechanisms involved [30]. The rest of the paper is organized as follows. Section II introduces the numerical methods calculating the relevant parameters and the characteristics of the electric-field noises. Considering different adsorbed atoms with strong or weak binding, we present the numerical results in Sec. III. Then a brief discussion is made in Sec. IV for the availability of detecting the electric-field noises using current technique with trapped-ion sensors. Finally, Sec. V draws the conclusion.

II. METHODS

A. Potential energy and electric dipole moment

In this paper, our calculations for the potential energies and electric dipole moments are conducted using the Vienna *ab initio* Simulation Package (VASP) [31,32], where a plane-wave basis is set by the projector augmented wave method [33,34]. The exchange-correlation interactions are described by the generalized gradient approximation in the Perdew-Burke-Ernzerhof formalism [35]. A plane-wave cutoff energy of 600 eV is employed, and the Γ -centered k -point mesh is chosen as $5 \times 5 \times 1$. The convergence criteria for the energy and force are set to be 1×10^{-6} eV and 0.01 eV/Å, respectively. Spin polarization and dipole correction are considered in all calculations. In addition, the VASPKIT program is used for charge density data processing [36].

The Cu(100) (2×2) supercell slab structure is constructed by cleaving the relaxed bulk Cu. The slab structure consists of six thick layers, in which the top four layers on the side of the slab are allowed to relax for modeling the atom adsorption and the bottom two layers as the bulk structure is fixed. Through tests the dipole moments reach reasonable converged values for Be, B, C, N, O, F, and Ar, when thickness of the vacuum layer is more than 25 Å as adopted in the latter calculations. For Li, a thickness of more than 40 Å is required for the dipole moment to converge reasonably.

The adsorption potential energy E_{ads} is calculated by

$$E_{\text{ads}} = E_{\text{surf+A}} - E_{\text{surf}} - E_{\text{A}}, \quad (1)$$

where $E_{\text{surf+A}}$ refers to the total energy of the Cu(100) (2×2) surface with an adsorption atom A , E_{surf} is the energy of the bare surface, and E_{A} represents the energy of an isolated adsorption atom. The change of the surface adsorption electric dipole moment $\Delta\mu$ is obtained by the x - y planar-averaged

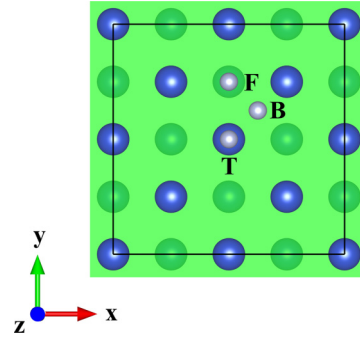


FIG. 1. Model for the atom adsorption (with 0.125-ML coverage) on the Cu(100) (2×2) surface at the top site (T), bridge site (B), and fcc site (F) by VESTA [39]. The blue large and silver small atoms represent Cu atoms and adatoms, respectively.

electron charge-density difference method [27,37,38]. The $\Delta\mu$ is given by

$$\Delta\mu = \int_a^{a+c} z \Delta\rho(z) dz, \quad (2)$$

where $\Delta\rho(z)$ is the x - y plane charge-density change upon the adatom adsorption, a is the length from the center of the slab to the surface, and c is the length of the $3/4$ cell.

There are three highly symmetric adsorption sites considered as the stable sites, as described by the adsorption structure model shown in Fig. 1. Table I presents the energies at different adsorption sites, in which the adatoms prefer to be adsorbed at the fcc site. This site is not the most stable adsorption site for the F adatom, as it exhibits a similar energy to the lowest one. For convenience, we choose the fcc site for comparisons as elucidated below. Results for the F adatom adsorbed at the bridge site are also presented for comparison in Appendix D.

B. Eigenenergies and wave functions

With the potential energy and the electric dipole moment with respect to the adsorption position z , we have solved the eigenenergies and wave functions of different vibrational

TABLE I. Adsorption energies for different adatoms and adsorption sites on the Cu(100) surface.

Adatom	Energy (eV)		
	T	B	F
Li	-1.857	-1.972	-2.141
Be	-1.584	-2.038	-2.957
B	-2.969	-3.903	-5.662
C	-3.171	-4.472	-6.424
N	-1.827	-3.231	-4.725
O	-3.449	-4.703	-5.407
F	-3.934	-4.397	-4.336
Ar ($\times 10^{-2}$)	-1.431	-1.421	-1.713

states using the static Schrödinger equation:

$$E|\psi(z)\rangle = \left(-\frac{\hbar^2}{2m} \frac{d^2}{dz^2} + U(z) \right) |\psi(z)\rangle, \quad (3)$$

where $U(z)$ is the potential energy calculated from the DFT, \hbar is the reduced Planck constant, and m is the mass of the adatom. In practice, $U(z)$ is fitted with a step size Δz and the kinetic operator is discretized with the same step size. Then the eigenenergies E and the wave functions $|\psi(z)\rangle$ can be obtained by direct diagonalization.

After acquiring the wave functions, we may calculate the expectations of the electric dipole moment with respect to different vibrational states as

$$\mu_i = \langle \psi_i(z) | \mu(z) | \psi_i(z) \rangle, \quad (4)$$

where $\mu(z)$ is the electric dipole moment for the adsorption position and $|\psi_i(z)\rangle$ is the wave function of the i th vibrational state obtained from Eq. (3).

C. Phonon-induced transition rate

In order to know the vibrational dynamics of the adatom and the consequent fluctuation of the electric dipole moment, we have calculated the phonon-induced transition rate following the work by Safavi-Naini *et al.* [12]. In that work, the transitions between different vibrational states are assumed to be caused by the emission and absorption of phonons in the bulk, resulting in the fluctuation of the electric dipole moment of the adatom. In this case, the phonon-induced transition rate between the i th and j th vibrational states can be evaluated with Fermi's "golden rule":

$$\Gamma_{i \rightarrow j} = \frac{\Delta\omega_{ij}}{2\pi\hbar v^3 \rho} \left| \langle j | \frac{d}{dz} U(z) | i \rangle \right|^2 [n(\Delta\omega_{ij}) + 1], \quad (5)$$

$$\Gamma_{j \rightarrow i} = \frac{\Delta\omega_{ij}}{2\pi\hbar v^3 \rho} \left| \langle j | \frac{d}{dz} U(z) | i \rangle \right|^2 n(\Delta\omega_{ij}), \quad (6)$$

where $\Delta\omega_{ij} = |E_i - E_j|/\hbar$, $n(\Delta\omega) = (e^{\hbar\Delta\omega/k_B T} - 1)^{-1}$ is the Bose-Einstein distribution, v is the averaged speed of sound in the surface material, and ρ is its bulk density. The approximation between the two lowest states indicates that the transition rate is sensitive to the quartic level difference [12]. For the Cu(100) surface, v and ρ are assumed to be 4760 m/s and 8.96 g/cm³, respectively [40].

D. Spectrum and autocovariance of the electric dipole moment

Using the eigenenergies, electric dipole moments, and phonon-induced transition rates as mentioned above, we are able to calculate the noise spectrum using [4]

$$S_E(\omega) = \frac{3\pi\sigma}{(4\pi\epsilon_0)^2 d^4} S_\mu(\omega), \quad (7)$$

$$S_\mu(\omega) = \text{Re} \int_0^t C(\tau) e^{-i\omega\tau} d\tau, \quad (8)$$

where the coefficient 1/2 in Eq. (7) has been dropped due to considering the time integral interval $[0, +\infty]$ rather than $[-\infty, +\infty]$. In our calculation, the system evolves within a finite time and thus the integral interval is set from zero to t in Eq. (8). σ is the coverage density of the adatoms, ϵ_0 is the

vacuum permittivity, and d is the ion-surface distance. $S_\mu(\omega)$ is the spectrum of the fluctuating electric dipole moment and can be calculated from the autocovariance $C(\tau)$. $C(\tau)$ is defined as [41]

$$C(\tau) = \overline{\mu(t)\mu(t+\tau)} \\ = \sum_{i,j} \mu_i \mu_j \rho_i(t) \rho_j^i(t+\tau), \quad (9)$$

where μ_i (μ_j) is the electric dipole moment of the i th (j th) vibrational state and $\rho_i(t)$ is the population when the system is in the i th vibrational state at time t . Similarly, $\rho_j^i(t+\tau)$ is the population when the system is in the j th vibrational state at time $t+\tau$, given that the system is in the i th vibrational state at time t . Assuming the autocovariance obeys the time translational symmetry, we may simplify Eq. (9) to be the following form:

$$C(\tau) = \sum_{i,j} \mu_i \mu_j \rho_i(0) \rho_j^i(\tau). \quad (10)$$

In order to know the time evolution of the population $\rho_j^i(\tau)$, we employ the incoherent master equation [12],

$$\dot{\rho}_j^i(\tau) = \sum_k M_{jk} \rho_k^i(\tau), \quad (11)$$

where the diagonal terms of the parameter M are defined as $M_{jj} = -\sum_{j \neq k} \Gamma_{j \rightarrow k}$ and the off-diagonal terms are $M_{jk} = \Gamma_{k \rightarrow j}$. Practically, the propagations of $\rho_j^i(\tau)$ are obtained with the initial conditions $\rho_j^i(0) = 1$ ($j = i$) and 0 ($j \neq i$), implying that the system evolves from the i th vibrational state. Then we calculate the autocovariance of the electric dipole moment using Eq. (10), where $\rho_i(0)$ is determined by the thermal equilibrium distribution.

III. NUMERICAL RESULTS

A. Comparison of various fitting methods

We first exemplify the C adatom to compare the spectra of the fluctuating dipole moment using different fitting methods. This is because the cryogenic approximation of the noise spectrum, determined by the quartic level difference, implies a strong sensitivity to the transition rate or the cutoff frequency (see Appendix B). Therefore, in order to solve the static Schrödinger equation and obtain reliable results, we should carefully treat the discrete energies calculated from the DFT. In what follows, we employ two potential formulas, i.e., the Morse potential $U(z) = D(1 - e^{-a(z-z_0)})^2 + D_0$ and the harmonic potential $U'(z) = k(z - z_0)^2 + D_0$, in our fitting. Figure 2(a) shows the fitting results and the corresponding wave function (of the 15th vibrational state) of the C adatom, in which another discrete data set of the potential energy [triangle in Fig. 2(a)] is calculated for comparison. We list the optimized parameters in Table II. We find that the harmonic potential leads to more stable results, whereas the Morse potential has smaller residual averages of squares ε^2 . Beyond the fitting range, both the Morse and harmonic potentials are not able to describe the realistic energy, i.e., the gray points. Fortunately, we find from Fig. 2 that the wave functions of the truncated vibrational state are adequately described within

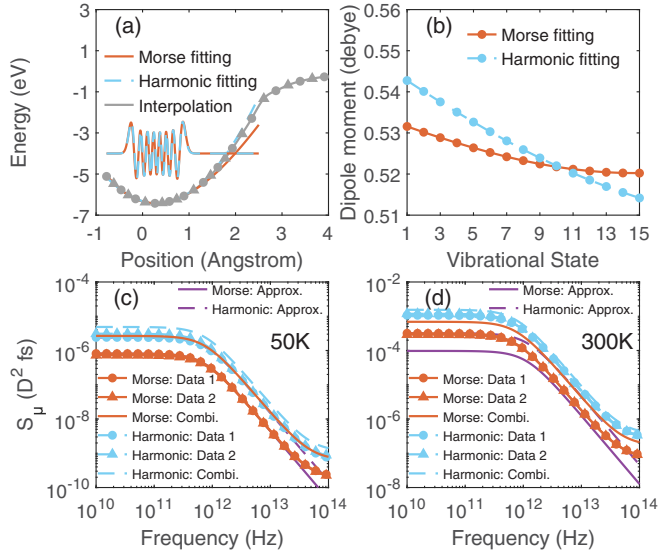


FIG. 2. (a) Potential energy and wave function (of the 15th vibrational state) of C adsorbed at the fcc site on the Cu(100) surface. Continuous lines of the potential are obtained from Morse-potential fitting (red solid line), harmonic-potential fitting (blue dashed line), and interpolation (gray solid line) of the first discrete data set (gray dots). (b) Expectations of the electric dipole moment of the lowest 15 vibrational states calculated from the fitting results of the first discrete data set and the interpolated origin dipole moment. (c), (d) Spectra of the dipole moment at (c) $T = 50$ K and (d) $T = 300$ K. Spectra of dotted and triangle lines are calculated from each data set, respectively. Spectra of lines without marks are obtained from combination of two data sets. For each data set and their combination, results of Morse- and harmonic-potential fitting are plotted as red solid lines and blue dashed lines, respectively. They are compared with the approximate results (purple lines).

the fitting range. Expectations of the electric dipole moment are plotted in Fig. 2(b), which are calculated from the fitting results of the first discrete data sets and exhibit difference.

We plot in Figs. 2(c) and 2(d) the spectra of the electric dipole moment for the cases of different temperatures, where the approximate results derived in Appendix B are also exhibited (purple lines). For both temperatures, the spectral lines of the harmonic-potential fits are more consistent with

TABLE II. Fitting parameters and residual averages of squares of the potential energies for C adsorbed on the Cu(100) surface.

Morse fitting	Data set 1	Data set 2	Combination
D (eV)	55.44	71.37	81.93
a (\AA^{-1})	0.1374	0.1223	0.1138
z_0 (\AA)	0.2859	0.2865	0.2885
D_0 (eV)	-6.421	-6.424	-6.423
$\varepsilon^2(10^{-4} \text{ eV}^2)$	0.04948	0.03867	0.08599
Harmonic fitting	Data set 1	Data set 2	Combination
k ($\text{eV}/\text{\AA}^2$)	1.081	1.029	1.053
z_0 (\AA)	0.3110	0.3107	0.3136
D_0 (eV)	-6.425	-6.418	-6.421
$\varepsilon^2(10^{-4} \text{ eV}^2)$	1.022	0.8981	1.293

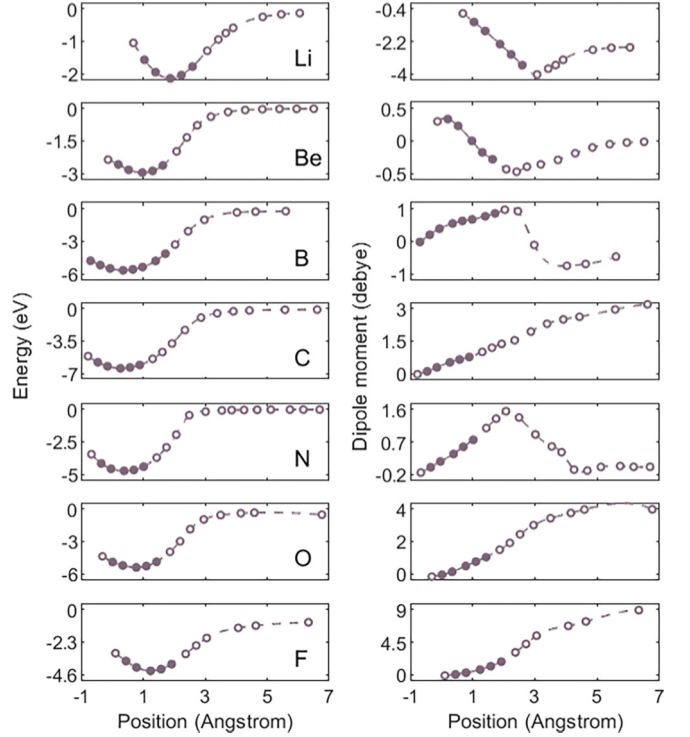


FIG. 3. Adsorption energies (left-side panels) and electric dipole moments (right-side panels) of different adatoms at the fcc site on the Cu(100) surface. Continuous lines are interpolations of the discrete data. The data of the energies excluded from fitting are marked with open circles and dashed lines. Corresponding data of the dipole moments are also marked with the same marks.

each other, and the intensities are larger than those of the Morse-potential fits. Moreover, we find that the approximate results, under the assumption of two levels, are consistent with the calculation results for the low temperature. However, the approximate results underestimate the spectral intensities whereas they slightly overestimate the cutoff frequency from the white noise to $1/f^2$ noise at $T = 300$ K. The latter case might be due to the lack of involving the higher-lying vibrational states. Moreover, the spectral lines rise at a higher frequency because of the finite step size in the calculations. More accurate results can be expected if smaller step size were employed in our calculations. In what follows, we adopt these two potential formulas to calculate the noise spectra and discuss more details about their difference.

B. Noise spectra of adatom vibration

To obtain the parameters of the master equation and the noise spectra, we first calculate the potential energies and the electric dipole moments of seven adatoms on the Cu(100) surface, as illustrated in Fig. 3. It is interesting to see that the surface can be penetrated by most of the adatoms, which can be understood by the exchange mechanism between the adatoms and the surface atoms in the surface diffusion [42]. In the region away from the surface, the potential energies exhibit an anharmonic property. We would utilize Morse and harmonic potentials to fit the discrete data in the subsequent calculations, and verify them by including the data far from

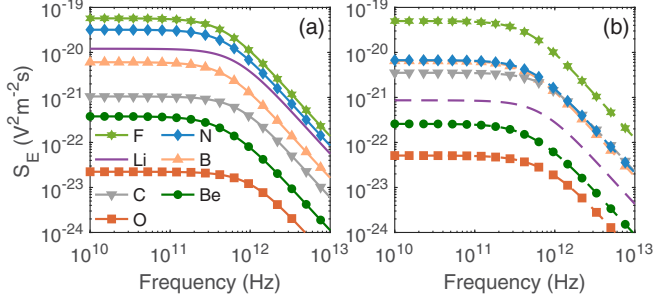


FIG. 4. Noise spectra of seven adatoms at the fcc site on the Cu(100) surface obtained from (a) the Morse-potential fitting (solid lines) and (b) the harmonic-potential fitting (dashed lines). The values of the characteristic parameters are the temperature $T = 300$ K, the coverage density of the adatoms 10^{18} m^{-2} , and the ion-surface separation distance $40 \text{ }\mu\text{m}$.

the surface. The exception is for the case of the weak-binding Ar adatom, in which the anharmonic potential leads to colored noise at low frequency, which will be discussed in the next section. Here we show the electric dipole moments we calculate in the right-hand side panels of Fig. 3, where the results are very different from the prediction derived from the image charge model, i.e., $\mu \sim z^{-4}$ [12]. We consider it to be caused by the complicated adatom-surface atoms interactions, as discussed previously [27]. In this case, we have used the interpolation method to acquire the continuous lines in the figure. In addition, we find that the results far from the equilibrium position for some of the adatoms have not converged. However, except for the O adatom, this does not impact the main conclusion in the following calculations because the data needed in our study are mainly concentrated near the stable adsorption sites (see discussions in Appendix C).

Based on the above results, we utilize the same methods as in the last section to calculate the noise spectra of the adatoms and investigate the influences of the adatom vibrations. Herein, the number of the vibrational states in our calculations is 15, the temperature is set as $T = 300$ K, the evolutionary time is chosen as $t = 0.1$ ns, and the step size $\Delta t = 0.1$ fs. In Fig. 4 we illustrate the results of different adatoms. However, all of the results here are much smaller than the experimental results [4], which needs further investigation. The spectral intensities exhibit visible differences for the Li, C, and the N adatoms, due to their small dissociation energies D as listed in Table III. The results calculated from

TABLE III. Optimized parameters of the potential energies with Morse-potential fitting.

	D (10^3 eV)	a (\AA^{-1})	z_0 (\AA)	D_0 (eV)	Da^2
Li	0.1382	0.0740	1.884	-2.136	0.7565
Be	14.59	0.006812	0.9442	-2.956	0.6772
B	4.057	0.01420	0.3525	-5.655	0.8183
C	0.05544	0.1374	0.2859	-6.421	1.047
N	0.01819	0.2258	0.3763	-4.736	0.9278
O	10.72	0.009715	0.7220	-5.402	1.012
F	3.005	0.01876	1.250	-4.326	1.057

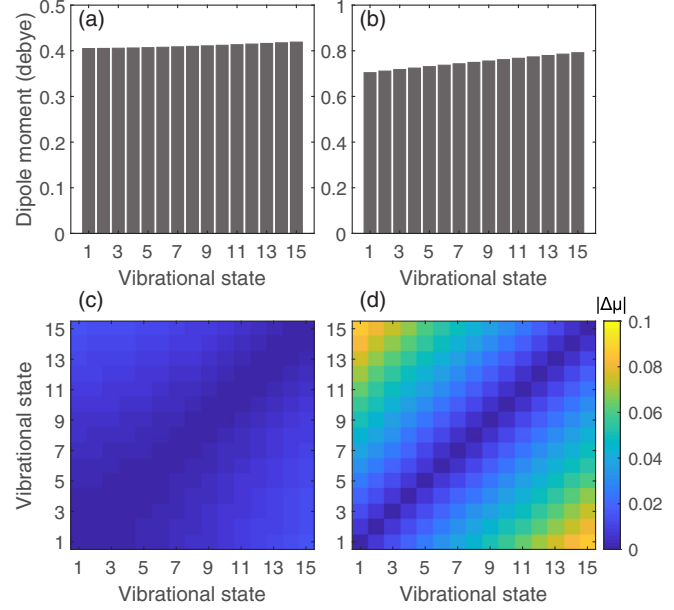


FIG. 5. Electric dipole moments of the lowest 15 vibrational states of the (a) O adatom and (b) F adatom. Their absolute differences are plotted in (c) for the O adatom and (d) for the F adatom. All these results are calculated from the Morse-potential fitting results.

the combined formula in Fig. 11 can help us confirm which calculation result is more reliable. For the C and N adatoms, a good agreement is found between the combined-formula and the harmonic-potential results. It indicates that the harmonic potential is adequate to describe the two adsorption systems, while the Morse-potential fits give rise to more anharmonic results and thus an underestimation or overestimation. For the Li adatom, the noise spectra with the combined formula is consistent with the Morse-potential one due to the slight anharmonicity of the adsorption energy.

We also find that the F adatom exhibits the largest intensity due to its strong electronegativity. In contrast, the O adatom has the weakest noise spectrum for both Morse- and harmonic-potential fittings, which can be understood as the differences among the electric dipole moments, reflecting the fluctuating intensity in the adatom vibrations. Figure 5 plots the electric dipole moments and their differences of the lowest 15 vibrational states of the O and F adatoms. Considering the viewpoint of the cryogenic approximation of the noise spectrum, we deem that the noise spectrum of the O adatom possessing smaller intensity than the F adatom is due to the quadratic dependence on the dipole moment difference $S_E \sim \Delta\mu^2$. We also check the calculations of the combined formula, namely, the results in Fig. 11, and find that this phenomenon and reason still hold.

Moreover, we observe very similar transition regions from white noise to $1/f^2$ noise in all these spectra, with the cutoff frequencies between 10^{11} and 10^{12} Hz. This can be understood as nearly the same vibrational energy scale or nearly the same fitting parameters Da^2 and k involved in the calculation, as listed in Tables III and IV. As mentioned above, the cutoff frequency is relevant to the quartic level difference or the quadratic Da^2 and k . As such, the noise spectra thus exhibit

TABLE IV. Optimized parameters of the potential energies with harmonic-potential fitting.

	k (eV/Å ²)	z_0 (Å)	D_0 (eV)
Li	0.7676	1.9016	-2.137
Be	0.6820	0.9446	-2.958
B	0.8187	0.3589	-5.6591
C	1.081	0.3110	-6.425
N	0.9643	0.4191	-4.740
O	1.018	0.7244	-5.405
F	1.064	1.254	-4.328

similar transition regions. To identify different adatoms, we have to focus on the spectral intensity or frequency scaling, because they are sensitive to complicated adsorption scenarios.

C. Colored feature stemming from the Ar adatom

Here we calculate another adsorption system, i.e., the Ar, on the Cu(100) surface. In this calculation, the anharmonic potential is considered to have a more important role due to the very weak interactions, which provides another possibility of the atomic adsorptions. On the other hand, because the Ar adatom is the residual in surface treatment experiments [9,10,17,21,22], we have interests in exploring the influence of this adatom on the electric-field noise after the surface treatments are made. Figures 6(a) and 6(b) plot the potential energy and electric dipole moment with respect to the position when the Ar is adsorbed on the fcc site. It should be mentioned that the van der Waals interaction is not taken into account in our calculation here and thus we mainly focus on presenting the qualitative properties.

Similar to the calculations in the last section, the potential energy and electric dipole moment are fitted to obtain the parameters. In order to consider the anharmonic potential, the energy is additionally fitted with a polynomial potential $U(z) = a/(z - z_0)^3 + D_0$ far away from the equilibrium position, keeping the same continuity and differentiability with the Morse potential at the critical point. For the electric dipole moment, rather than using interpolation, the multiple-polynomials function is adopted for fitting in order to predict the value away from the equilibrium position, for which the details can be found in Appendix A and their results

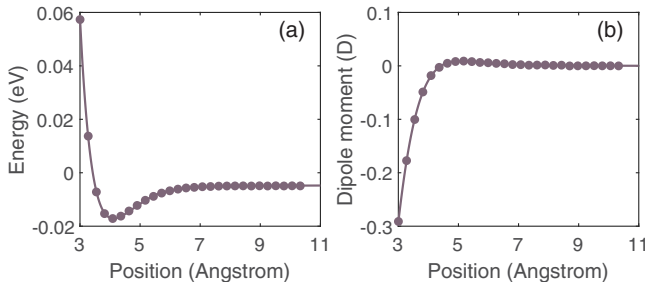


FIG. 6. (a) Potential energy and (b) electric dipole moment with respect to the adsorption position for Ar adsorbed at the fcc site on the Cu(100) surface.

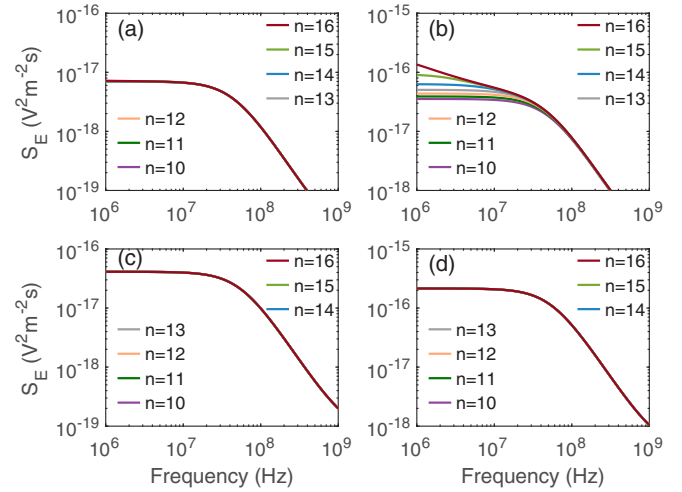


FIG. 7. Noise spectra for Ar adsorbed at the fcc site on the Cu(100) surface with the temperature of (a) $T = 10$ K and (b) $T = 20$ K. Results obtained from harmonic-potential approximation are given in (c) for $T = 10$ K and (d) for $T = 20$ K. Legends are the number of the calculated vibrational states. The result with the highest truncation covers other lines in (a), (c), and (d). The coverage density of the adatoms is 10^{18} m^{-2} and the ion-surface separation distance is $40 \mu\text{m}$.

are shown in Figs. 6(a), 6(b), and 9. Then, the spectra of electric-field noise with different temperatures and truncations are calculated and depicted in Figs. 7(a) and 7(b). Herein, the evolutionary time and step size are adopted as $t = 10 \mu\text{s}$ and $\Delta t = 0.01 \text{ ns}$, respectively. Other conditions, such as the coverage density and the ion-surface separation distance, are the same as in the last section. We first focus on the low-temperature results with $T = 10$ K in Fig. 7(a), in which the number of the calculated vibrational states n is chosen from 10 to 16. It is found that the calculated results seem to converge with increasing truncation, and the spectral lines have little changes even with higher truncation. However, a rise of the spectral line can be spotted when considering a higher temperature of $T = 20$ K as shown in Fig. 7(b), which implies an unusual colored feature beyond the white noise at low-frequency region. For small truncations, the spectral lines exhibit the white noise at low frequency, but the intensity has not reached its convergence. While further increasing the truncation, the colored feature appears in the counterpart region. Moreover, it can be seen that the higher additional vibrational states only change the spectral line of the lower frequency. For $n = 16$, the white noise completely disappears even at a small frequency 10^6 Hz . For higher truncation, calculation becomes harder due to the rapid increase of the dimension.

It is still a question whether the colored feature is caused by the imprecision of the numerical calculation. Although this can be partially clarified by the fact that the parameters for the master equation are calculated from the direct diagonalization, we try to provide a different viewpoint to support the reliability and find the possible mechanism. Actually, the low frequency makes us relate the colored feature to the long time or the small energy scale of the vibrational dynamics. Therefore, we consider an approximate harmonic potential to

calculate the corresponding noise spectra for comparison. The harmonic potential considered here is the expansion of the fitted function. In this case, the approximation would not change the low-lying vibrational states, but the anharmonic property away from the equilibrium position vanishes. In addition, the expectations of the dipole moment are obtained from interpolation for convenience. In Figs. 7(c) and 7(d), the noise spectra are illustrated and exhibit good self-consistencies. For both cases, all of the spectral lines are in agreement with each other. Due to this fact, we consider that the colored feature is caused by the thermal activation of the high-lying vibrational states of the anharmonic potential. For such a weak-binding adsorption system, approaching a high vibrational state in a large coordinate space with $z = 40 \text{ \AA}$ for $n = 15$ or $z = 70 \text{ \AA}$ for $n = 16$ is required for the wave function. Other mechanisms might be relevant to the adatom vibrations, leading to more complicated spectra. Nevertheless, the calculated results provide us an unusual picture in such a simple adsorption scheme. Moreover, to observe the colored feature, we may measure the spectral frequency scaling by changing the temperature. Although the argon adatom existing as residual of the surface treatment has never been taken as the main factor of the noises, we still consider from our calculation that this is an interesting conjecture to single out the Ar adatom from other factors in the treatment of the colored feature.

IV. DISCUSSION

As mentioned in the Introduction, the electric-field noises leading to heating are the main detrimental factor for precision manipulation and scalability of the qubits in trapped-ion systems. On the other hand, the laser-cooled trapped ions extremely sensitive to the electric-field noises make them excellent sensors in the detection of the modification and fluctuation of external electric fields. This noise detection plays a role in a wide variety of experiments, even going beyond the ion traps to offer new ways to analyze surfaces to complement the existing surface-science toolbox [4,43,44].

However, it is still an open question how trapped-ion sensors can work better for detecting the electric-field noise and the relevant surface adsorption. For the monatomic adsorption with low coverage density and low diffusion coefficient, the adatom vibration plays the main role. Putting aside other spectral properties, however, we find the intensities of the noise spectra we calculated above are too small to be detected experimentally. With respect to the previous review paper, the spectral intensities detected in the experiments range from 10^{-12} to $10^{-9} \text{ V}^2 \text{ m}^{-2} \text{ s}$ with an ion-surface separation of 40 \mu m [4]. Our paper shows that the Ar adatom leads to a noise intensity of $10^{-16} \text{ V}^2 \text{ m}^{-2} \text{ s}$ which is smaller than the experimental results. The other adatoms (with the intensity from 10^{-23} to $10^{-19} \text{ V}^2 \text{ m}^{-2} \text{ s}$) have difficulty meeting the experimental intensities. One of the reasons might be the density of states (DOS) assumed as an Ohmic spectrum, as in Eqs. (5) and (6). Herein, we change the DOS from sub-Ohmic spectrum to super-Ohmic spectrum. Specifically, $\Delta\omega$ in Eqs. (5) and (6) is replaced with $\Delta\omega^s \Delta\omega_{\max}^{1-s}$, where $\Delta\omega_{\max}$ is the cutoff frequency referring to the maximal level difference among the calculated vibrational states. In this case, the sub-Ohmic, Ohmic, and super-Ohmic spectra are

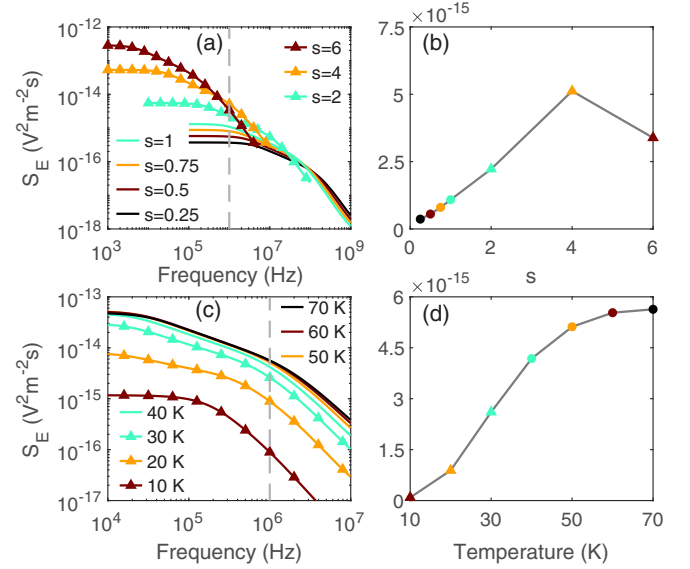


FIG. 8. Electric-field noise for Ar adsorbed at the fcc site on the Cu(100) surface with changed DOS. (a) Noise spectra with respect to s , in which the temperature $T = 50 \text{ K}$ and their spectral intensities at 1 MHz are plotted in (b). (c) Noise spectra with respect to the temperature, in which $s = 4$ and the spectral intensities at 1 MHz are plotted in (d). The coverage density of the adatoms is 10^{18} m^{-2} and the ion-surface separation distance is 40 \mu m .

specified by $s < 1$, $s = 1$, and $s > 1$, respectively. Figure 8(a) plots the change of the noise spectrum with respect to s and Fig. 8(b) shows the spectral intensity at 1 MHz . Here all of the results are calculated with the number of the vibrational states $n = 16$ and the temperature $T = 50 \text{ K}$. We find that the sub-Ohmic spectrum hardly influences the line shape of the noise spectrum comparing with the result of $s = 1$. However, for the super-Ohmic spectrum, the cutoff frequency from the white noise to $1/f^2$ noise decreases and the spectral intensity is enhanced. Figure 8(b) shows the highest intensity of about $5 \times 10^{-15} \text{ V}^2 \text{ m}^{-2} \text{ s}$ at 1 MHz , which is closer to current capability of the experimental detection. In Fig. 8(c), $s = 4$ with the highest intensity is adopted to exhibit the influence of the temperature. The truncated vibrational state is also $n = 16$, which is however insufficient for those high-temperature cases. We find that the colored feature also appears but shifts to the lower-frequency region. The spectral intensity exhibits an increasing trend while raising the temperature, and then begins to saturate as shown in Fig. 8(d).

According to our calculation, there are some other reasons as follows. The first is that the complicated adsorption vibrations are not taken into account. Many realistic adsorption species interact with the surface atoms and have more complicated vibrational modes with different energy scales [45,46]. Furthermore, when the adatoms form into clusters, they might exhibit a collective dynamics and possess lower frequencies due to the weak molecule or cluster-surface interactions. In these cases, the low cutoff frequency equally increases the intensity of the noise spectrum. Actually, a similar case has been considered, as the calculated noise spectra resulting from in-plane vibrations are found to have larger spectral intensities than those of the out-of-plane results [27]. Enlightened by the

fact that the differences among the electric dipole moments would impact the noise spectra, another possible reason is the correlation of the electric dipole moments. In the present paper, the fluctuation of each dipole moment is treated as independent dynamics. However, other bathlike adatoms might induce electric dipole moment enhancement (or reduction) and a correlation effect contributing to the spectroscopy. In a word, these considerations suggest to us to focus on the mechanisms of complicated molecular or cluster vibrations and to take the interactions among the adatoms into account.

Furthermore, we have noticed recent efforts exploring the detection of noise spectra using harmonic oscillators [47–49]. The basic ideas in these works are enacted on the harmonic oscillators with preparation of cold initial states and variation of resonance frequencies, which are directly relevant to the laser-cooled ions confined in electromagnetic fields. In this context, the accuracy of these methods is mainly limited by the temperature of the ions, e.g., sideband cooling of the trapped ions is the prerequisite of the techniques demonstrated. Nevertheless, the intrinsic noise spectra of the ion-trap potentials were experimentally identified and demonstrated [48,49]. Being not limited to the motional heating, the electric-field noise stemming from the adsorption surface is also a possible reason for the fluctuation of the secular frequency and thus decoherence in the ion trap [50]. Therefore, these methods manifest their practical potential for high-precision trapped-ion detection in adsorption science.

V. CONCLUSION

In this paper, we have calculated the electric-field noise for the monatomic adsorptions on the Cu(100) surface. Taking the nuclear vibrations into account, we have performed the DFT calculations to obtain the relevant parameters required for the incoherent master equation and the consequent vibrational dynamics. Two kinds of adatoms, including strong- and weak-binding ones, were adopted as calculated adatoms in the discussion of their spectral intensities and frequency scalings. For the latter, we find that the strong-binding adatoms exhibit similar frequency scalings because their fitting parameters have no significant differences. On the other hand, the weak-binding adatom, which was exemplified as Ar in our calculations, showed a colored feature in the low-frequency region with increasing temperature and the truncation of the vibrational state. In comparison with the harmonic approximate results, this feature was considered to be caused by the vibrational dynamics of the high-lying states in an anharmonic potential. We have not considered in our paper other mechanisms, which would couple to the adatom vibrations or cover this effect, influencing the colored feature. Nevertheless, the results in the present paper provide us a different viewpoint of the extremely weak-binding adsorption systems.

Some of the authors of the present paper have tried a preliminary detection of the electric-field noises in a surface electrode trap [51] by a single-atom sensor made of a single trapped ion, where the electric-field noises were probed in the order of magnitude of 10^{-10} V²/m² Hz and the detected sensitivity is hopefully further improved [52]. The key point of this sensor is the trapped ion behaving as an injection-locked phonon laser, i.e., an amplitude-amplified harmonic oscillator,

which is quite sensitive to the external disturbance, as reported previously [53–58]. This sensitive feature of the phonon laser was recently reflected in the probe of the ac electric-field fluctuation in the surface electrode trap, achieving the detection sensitivity of yocto-newton degrees of magnitude of ac electric force [59]. We will next focus on detecting the surface adsorptions and clarifying the mechanisms of complicated molecular or cluster vibrations. Therefore, the interactions among the adatoms will be considered in the present calculated scheme in our future work.

ACKNOWLEDGMENTS

This work was supported by the Special Project for Research and Development in Key Areas of Guangdong Province (Grant No. 2020B0303300001), the Key Lab of Guangzhou for Quantum Precision Measurement (Grant No. 202201000010), and the National Natural Science Foundation of China (Grants No. U21A20434, No. 91833305, and No. 11974118).

J.Z. and X.-T.Y. contributed equally to this work.

APPENDIX A: FITTING POTENTIAL ENERGIES AND ELECTRIC DIPOLE MOMENTS

As mentioned in the main text, for the strong-binding adatoms, we have fitted their potential energies with the Morse and harmonic potentials. Corresponding results are listed in Tables II–IV. For the Ar adatom, a combination of the Morse and polynomial potentials is adopted, which keeps the same continuity and differentiability at the critical point. For clearer exhibition, the combination can be written as

$$U(z) = \begin{cases} D(1 - e^{-a(z-z_0)})^2 + D_0, & z \leq 5.443 \text{ \AA} \\ a/(z - z'_0)^3 + D'_0, & z > 5.443 \text{ \AA} \end{cases} \quad (\text{A1})$$

For the Morse potential part, the parameters are adopted as $D = 0.01489$ eV, $a = 1.056 \text{ \AA}^{-1}$, $z_0 = 4.115 \text{ \AA}$, and $D_0 = -0.01711$ eV. For another part, the fitting parameters are $a = -0.03285$ eV \AA^3 , $z'_0 = 3.415 \text{ \AA}$, and $D'_0 = -0.004704$ eV.

Similarly, in order to predict the electric dipole moment beyond the DFT results, we have employed the combination of the polynomial functions to fit the discrete data. Since the concrete form of the dipole moment is not clear, we changed the number of terms and exponents and found an appropriate formula to describe the DFT results:

$$\mu(z) = \begin{cases} a_1/z^3 + b_1/z^5 + c_1/z^6 + \mu_0, & z \leq 4.6325 \text{ \AA} \\ a_2/z^7 + b_2/z^8, & z > 4.6325 \text{ \AA} \end{cases}, \quad (\text{A2})$$

where the fitting parameters read $a_1 = 33.37 \text{ D \AA}^3$, $b_1 = -857.4 \text{ D \AA}^5$, $c_1 = 1.518 \times 10^3 \text{ D \AA}^6$, and $\mu_0 = -0.08174 \text{ D}$ for the upper function. For the bottom one, $a_2 = 5.769 \times 10^3 \text{ D \AA}^7$ and $b_2 = -2.553 \times 10^4 \text{ D \AA}^8$. From Fig. 9 we know the fitting results have a good description for the discrete data, even for those small electric dipole moments.

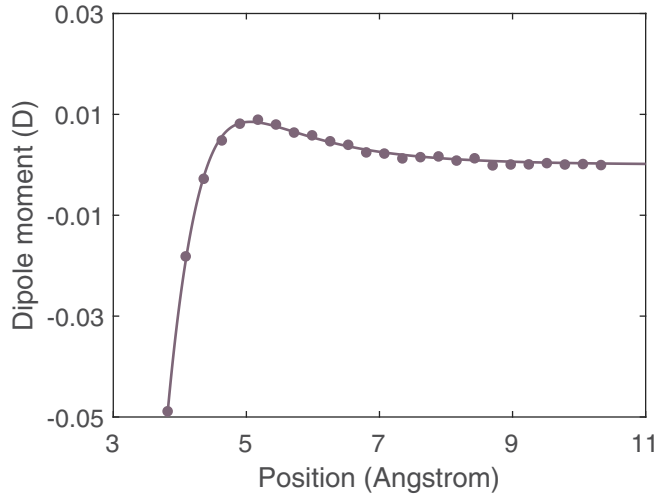


FIG. 9. Detailed view of the electric dipole moment and fitting result with respect to the adsorption position for Ar adsorbed at the fcc site on the Cu(100) surface.

APPENDIX B: APPROXIMATE FORMULA OF THE NOISE SPECTRUM AT CRYOGENIC TEMPERATURE

In this section, we derive the approximate formula of the electric-field noise at cryogenic temperature with the methods mentioned in the main text. Considering the two lowest vibrational states, the transition matrix in the master equation can be simplified as

$$M = \begin{pmatrix} -\Gamma_{01} & \Gamma_{10} \\ \Gamma_{01} & -\Gamma_{10} \end{pmatrix}. \quad (\text{B1})$$

Then the populations are

$$\rho_1(t) = ce^{-(\Gamma_{01} + \Gamma_{10})t} + \frac{\Gamma_{10}}{\Gamma_{01} + \Gamma_{10}}, \quad (\text{B2})$$

$$\rho_2(t) = -ce^{-(\Gamma_{01} + \Gamma_{10})t} + \frac{\Gamma_{01}}{\Gamma_{01} + \Gamma_{10}} \quad (\text{B3})$$

exhibiting an exponential decay. Since the system always evolves to its thermal equilibrium within a long enough time, the constant terms in the population obey the Boltzmann distribution and can be written as

$$\frac{\Gamma_{10}}{\Gamma_{01} + \Gamma_{10}} = \frac{1}{1 + e^{-\Delta E/k_B T}}, \quad (\text{B4})$$

$$\frac{\Gamma_{01}}{\Gamma_{01} + \Gamma_{10}} = \frac{e^{-\Delta E/k_B T}}{1 + e^{-\Delta E/k_B T}}, \quad (\text{B5})$$

where ΔE is the energy difference between the two lowest vibrational states.

Assuming that the initial state is in the ground state [$\rho_0(0) = 1$] and the excited state [$\rho_1(0) = 1$], respectively, we acquire the autocovariance of the electric dipole moment $C(t)$ using Eq. (10):

$$C(t) = \frac{\Delta\mu^2 e^{-\Delta E/k_B T}}{(1 + e^{-\Delta E/k_B T})^2} e^{-(\Gamma_{01} + \Gamma_{10})t} + \frac{(\mu_0 + \mu_1 e^{-\Delta E/k_B T})^2}{(1 + e^{-\Delta E/k_B T})^2}. \quad (\text{B6})$$

Herein, $\Delta\mu = |\mu_1 - \mu_0|$ is the difference between the dipole moments of the vibrational states. Neglecting the constant

TABLE V. Atomic highest occupied energy levels and lowest unoccupied energy levels of Li, Be, B, C, N, O, F, and Ar.

Adatom	Highest occupied energy levels (eV)	Lowest unoccupied energy levels (eV)
Li	-3.260 ($2s^1$)	-1.360 ($2s^2$)
Be	-5.613 ($2s^2$)	-2.020 ($2p^1$)
B	-4.228 ($2p^1$)	-3.632 ($2p^2$)
C	-6.099 ($2p^2$)	-5.573 ($2p^3$)
N	-8.296 ($2p^3$)	-4.129 ($2p^4$)
O	-8.795 ($2p^4$)	-6.424 ($2p^5$)
F	-11.082 ($2p^5$)	-9.482 ($2p^6$)
Ar	-10.268 ($3p^6$)	-0.482 ($4s^1$)

term of the autocovariance, the noise spectrum can be thus calculated by applying the Fourier transformation:

$$S_E(\omega) = \frac{\Delta\mu^2 e^{-\Delta E/k_B T}}{(1 + e^{-\Delta E/k_B T})^2} \frac{(\Gamma_{01} + \Gamma_{10})}{\omega^2 + (\Gamma_{01} + \Gamma_{10})^2}. \quad (\text{B7})$$

For further approximations, we set $\Gamma_{01} = 0$ and $1 + e^{-\Delta E/k_B T}$ in the denominator to be 1, taking the condition of the cryogenic temperature into account. Finally we have

$$S_\mu(\omega) = \Delta\mu^2 e^{-\Delta E/k_B T} \frac{\Gamma_{10}}{\omega^2 + \Gamma_{10}^2}, \quad (\text{B8})$$

which is consistent with the result in Ref. [12]. Due to the time integral interval $[0, +\infty]$ rather than $[-\infty, +\infty]$ in this paper, the result becomes half of the counterpart in that work.

APPENDIX C: CHARGE TRANSFER OF THE ADSORPTION SYSTEMS

In general, the amount of charge transfer between atoms gradually decreases to zero as the adsorption distance increases. However, we find there are still remarkable charge transfers beyond 10 Å for Li, B, C, O, and F. As examples, we calculate the x - y planar-averaged electron charge-density difference of Li, N, and F adsorption systems along the z -axis direction shown in Fig. 10, which to some extent reflects the charge transfers. Regarding this issue, we have calculated atomic highest occupied energy levels and lowest unoccupied energy levels of Li, Be, B, C, N, O, F, and Ar relative to the vacuum level, as listed in Table V. Of note, it is not proper to compare these orbital energies of valence electrons directly with the experimental values because the pseudopotentials are employed in the VASP calculations.

In our calculation the work function of the Cu(100) surface is 4.43 eV, in line with the experimental value of 4.59 eV [60]. It is clear that the free atoms Li and B have higher occupied levels comparing with the Fermi energy level of the Cu(100) surface. As a result, VASP wrongly transfers the higher-level electrons from Li and B atoms to the Cu(100) surface, even though they are far away from the surface. Correspondingly, for adsorption systems of C, O, and F, due to the lower unoccupied energy level of the free atoms, electrons are wrongly transferred from the Cu(100) surface to the atoms

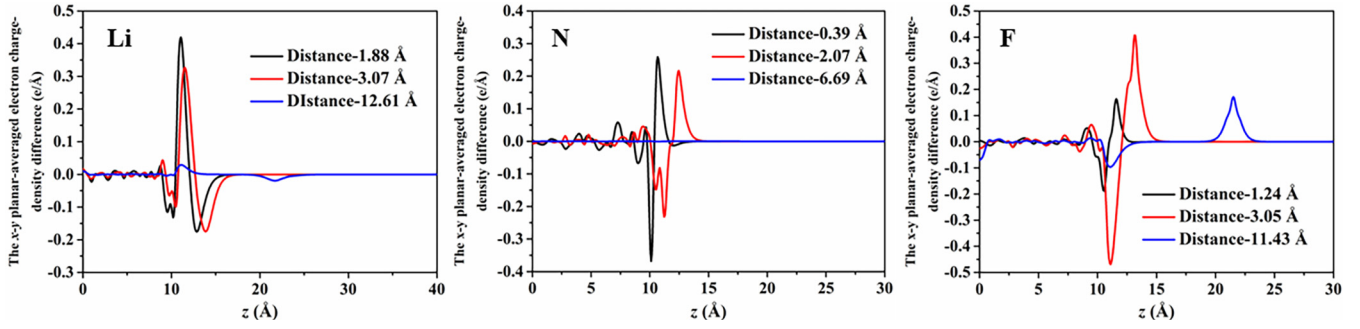


FIG. 10. x - y planar-averaged electron charge-density difference at different adsorption positions for Li, N, and F adsorbed on the Cu (100) surface.

far away even if they should not have interaction with the surface.

These unreasonable charge transfers result in the irregular convergence of the magnetic moment and adsorption energy of the corresponding adsorption systems. So far, it is not easy to solve the irregular convergence of Li, B, C, N, O, and F when far from the surface due to the incorrect occupation of the electronic energy levels. Nevertheless, the data needed in our paper are mainly concentrated near the stable adsorption sites. Herein, we take the adsorption systems Li, C, N, and O as examples and use a combined formula to fit the adsorption energies:

$$U(z) = \begin{cases} D(1 - e^{-a(z-z_0)})^2 + D_0, & z \leq z_c \\ b_1/z^{n_1} + b_2/z^{n_2} + D'_0, & z > z_c \end{cases} \quad (\text{C1})$$

It should be mentioned that the fitting results using the combined formula could not entirely describe the energies near the stable absorption sites, but give us a perspective of the influences of those data for the adatoms far from the surface. The fitting parameters are listed in Table VI. Then, corresponding noise spectra are plotted in Fig. 11 and compared with the results in Fig. 4, for which only the data near the stable adsorption site are taken into account. We find for Li, C, and N adatoms, the good agreement can be found for the Morse- or harmonic-potential fits, indicating the above conjecture is appropriate. Moreover, the combined-formula spectrum of the O adatom has a larger intensity than both

TABLE VI. Optimized parameters of the potential energies with combined-potential fitting.

	Li	C	N	O
D (10^3 eV)	0.1356	8.133	2.117	2.889
a (10^{-2} \AA^{-1})	7.016	1.137	2.278	1.930
z_0 (\AA)	1.903	0.3247	0.4186	0.6820
D_0 (eV)	-2.117	-6.419	-4.775	-5.417
b_1 (eV \AA^{n_1})	-33.07	-15.39	-3610	-4.206
b_2 (eV \AA^{n_2})	-111.0	-170.6	20331	-369.7
n_1	3	3	9	3
n_2	6	6	12	6
D'_0 (10^{-3} eV)	-3.183	-7.209	-1.972	-201.6
z_c (\AA)	3.069	2.349	2.067	2.520

Morse- and harmonic-potential results. It means that the potential tail has an influence and both the two potentials are not adequate to describe this adsorption system. We have also checked other adatoms and found good consistencies.

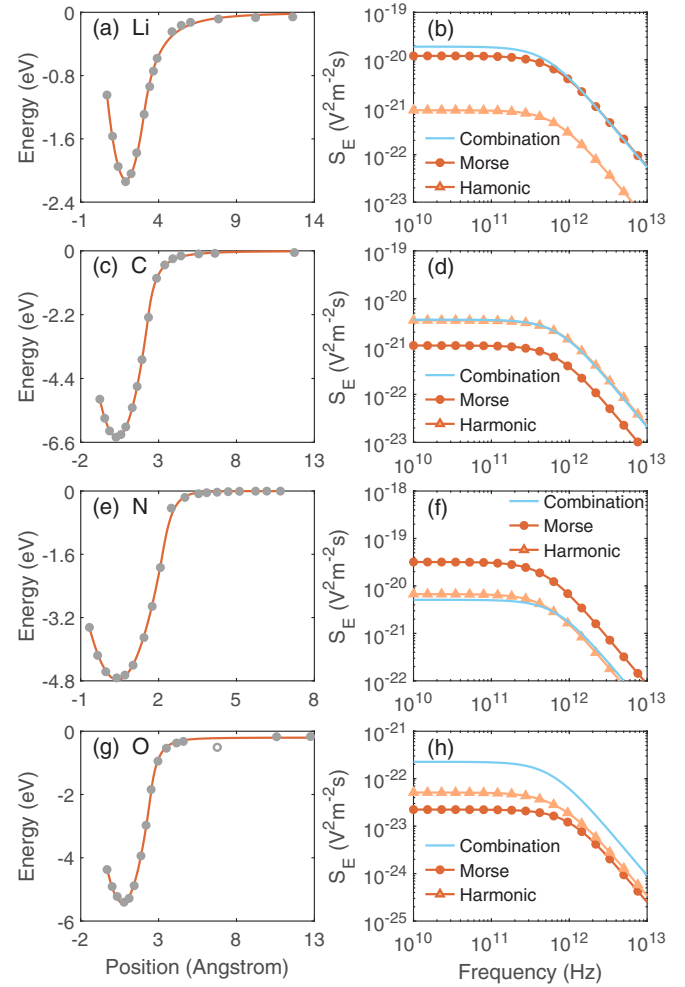


FIG. 11. Adsorption energies and their fitting results using a combined formula of the (a) Li, (c) C, (e) N, and (g) O adatom, respectively. The data excluded from the fitting are marked by open circles. (b), (d), (f), (h) Corresponding noise spectra calculated from the fitting results, compared with the results in Fig. 4.

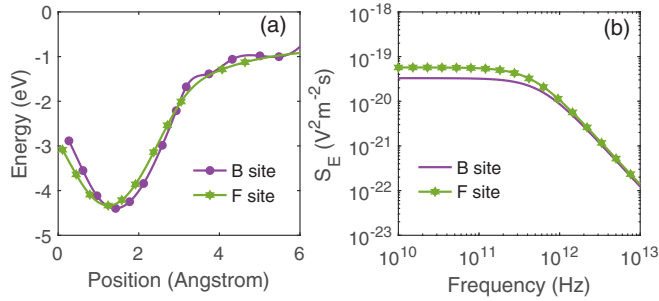


FIG. 12. (a) Adsorption potential energies of the F adatom at the bridge site (purple dotted line) and fcc site (green hexagram line) on the Cu(100) surface. Continuous lines are interpolations of the discrete data. (b) Noise spectra of the F adatom on the Cu(100) surface. Purple lines are the result at the bridge site and green lines are at the fcc site, both of which are calculated from the Morse-potential fits.

APPENDIX D: COMPARISON OF NOISE SPECTRA FOR THE F ADATOM AT DIFFERENT ADSORBED SITES

The bridge site, rather than the fcc site, is actually the most stable adsorption site for the F adatom on the Cu(100) surface. Herein, results including potential energies and noise spectra for the bridge and fcc site are given in Fig. 12. Results of the bridge site are seen to have no significant differences from the other potential line and we use the Morse potential to fit them. The parameters are obtained as $D = 87.66$ eV, $a = 0.1162$ Å⁻¹, $z_0 = 1.418$ Å, and $D_0 = -4.387$ eV. Then the calculation spectra with a temperature of $T = 300$ K are illustrated in Fig. 12(b), where the results of the bridge site exhibit slightly smaller intensities than those of the fcc site.

- [1] C. D. Bruzewicz, J. Chiaverini, R. McConnell, and J. M. Sage, Trapped-ion quantum computing: Progress and challenges, *Appl. Phys. Rev.* **6**, 021314 (2019).
- [2] R. Blatt and C. F. Roos, Quantum simulations with trapped ions, *Nat. Phys.* **8**, 277 (2012).
- [3] C. Monroe, W. C. Campbell, L.-M. Duan, Z.-X. Gong, A. V. Gorshkov, P. Hess, R. Islam, K. Kim, N. M. Linke, G. Pagano *et al.*, Programmable quantum simulations of spin systems with trapped ions, *Rev. Mod. Phys.* **93**, 025001 (2021).
- [4] M. Brownnutt, M. Kumph, P. Rabl, and R. Blatt, Ion-trap measurements of electric-field noise near surfaces, *Rev. Mod. Phys.* **87**, 1419 (2015).
- [5] K. R. Brown, J. Chiaverini, J. M. Sage, and H. Häffner, Materials challenges for trapped-ion quantum computers, *Nat. Rev. Mater.* **6**, 892 (2021).
- [6] Q. A. Turchette, B. King, D. Leibfried, D. Meekhof, C. Myatt, M. Rowe, C. Sackett, C. Wood, W. Itano, C. Monroe *et al.*, Heating of trapped ions from the quantum ground state, *Phys. Rev. A* **61**, 063418 (2000).
- [7] D. Leibfried, R. Blatt, C. Monroe, and D. Wineland, Quantum dynamics of single trapped ions, *Rev. Mod. Phys.* **75**, 281 (2003).
- [8] D. Allcock, L. Guidoni, T. Harty, C. Ballance, M. Blain, A. Steane, and D. Lucas, Reduction of heating rate in a micro-fabricated ion trap by pulsed-laser cleaning, *New J. Phys.* **13**, 123023 (2011).
- [9] D. A. Hite, Y. Colombe, A. C. Wilson, K. R. Brown, U. Warring, R. Jördens, J. D. Jost, K. McKay, D. Pappas, D. Leibfried *et al.*, 100-Fold Reduction of Electric-Field Noise in an Ion Trap Cleaned with *In Situ* Argon-Ion-Beam Bombardment, *Phys. Rev. Lett.* **109**, 103001 (2012).
- [10] N. Daniilidis, S. Gerber, G. Bolloten, M. Ramm, A. Ransford, E. Ulin-Avila, I. Talukdar, and H. Häffner, Surface noise analysis using a single-ion sensor, *Phys. Rev. B* **89**, 245435 (2014).
- [11] K. McKay, D. Hite, Y. Colombe, R. Jördens, A. Wilson, D. Slichter, D. Allcock, D. Leibfried, D. Wineland, and D. Pappas, Ion-trap electrode preparation with Ne⁺ bombardment, [arXiv:1406.1778](https://arxiv.org/abs/1406.1778).
- [12] A. Safavi-Naini, P. Rabl, P. Weck, and H. Sadeghpour, Microscopic model of electric-field-noise heating in ion traps, *Phys. Rev. A* **84**, 023412 (2011).
- [13] A. Safavi-Naini, E. Kim, P. Weck, P. Rabl, and H. Sadeghpour, Influence of monolayer contamination on electric-field-noise heating in ion traps, *Phys. Rev. A* **87**, 023421 (2013).
- [14] E. Kim, A. Safavi-Naini, D. Hite, K. McKay, D. Pappas, P. Weck, and H. Sadeghpour, Electric-field noise from carbon-adatom diffusion on a Au(110) surface: First-principles calculations and experiments, *Phys. Rev. A* **95**, 033407 (2017).
- [15] M. Kumph, C. Henkel, P. Rabl, M. Brownnutt, and R. Blatt, Electric-field noise above a thin dielectric layer on metal electrodes, *New J. Phys.* **18**, 023020 (2016).
- [16] M. Teller, D. A. Fioretto, P. C. Holz, P. Schindler, V. Messerer, K. Schüppert, Y. Zou, R. Blatt, J. Chiaverini, J. Sage *et al.*, Heating of a Trapped Ion Induced by Dielectric Materials, *Phys. Rev. Lett.* **126**, 230505 (2021).
- [17] J. Sedlacek, J. Stuart, D. Slichter, C. Bruzewicz, R. McConnell, J. Sage, and J. Chiaverini, Evidence for multiple mechanisms underlying surface electric-field noise in ion traps, *Phys. Rev. A* **98**, 063430 (2018).
- [18] C. Bruzewicz, J. Sage, and J. Chiaverini, Measurement of ion motional heating rates over a range of trap frequencies and temperatures, *Phys. Rev. A* **91**, 041402 (2015).
- [19] J. Sedlacek, A. Greene, J. Stuart, R. McConnell, C. Bruzewicz, J. Sage, and J. Chiaverini, Distance scaling of electric-field noise in a surface-electrode ion trap, *Phys. Rev. A* **97**, 020302 (2018).
- [20] D. An, C. Matthiesen, E. Urban, and H. Häffner, Distance scaling and polarization of electric-field noise in a surface ion trap, *Phys. Rev. A* **100**, 063405 (2019).
- [21] D. Hite, K. McKay, and D. P. Pappas, Surface science motivated by heating of trapped ions from the quantum ground state, *New J. Phys.* **23**, 103028 (2021).
- [22] M. Berlin-Udi, C. Matthiesen, P. T. Lloyd, A. M. Alonso, C. Noel, B. Saarel, C. A. Orme, C.-E. Kim, A. J. Nelson, K. G. Ray *et al.*, Changes in electric field noise due to thermal transformation of a surface ion trap, *Phys. Rev. B* **106**, 035409 (2022).
- [23] K. Lakhmankiy, P. Holz, D. Schärtl, B. Ames, R. Assouly, T. Monz, Y. Colombe, and R. Blatt, Observation of supercon-

- ductivity and surface noise using a single trapped ion as a field probe, *Phys. Rev. A* **99**, 023405 (2019).
- [24] P. C. Holz, K. Lakhmanskiy, D. Rathje, P. Schindler, Y. Colombe, and R. Blatt, Electric-field noise in a high-temperature superconducting surface ion trap, *Phys. Rev. B* **104**, 064513 (2021).
- [25] H. Jooya, K. McKay, E. Kim, P. Weck, D. Pappas, D. Hite, and H. Sadeghpour, Mechanisms for carbon adsorption on Au(110)-(2 × 1): A work function analysis, *Surf. Sci.* **677**, 232 (2018).
- [26] H. Jooya, X. Fan, K. McKay, D. Pappas, D. Hite, and H. Sadeghpour, Crystallographic orientation dependence of work function: Carbon adsorption on Au surfaces, *Mol. Phys.* **117**, 2157 (2019).
- [27] K. G. Ray, B. M. Rubenstein, W. Gu, and V. Lordi, Van der Waals-corrected density functional study of electric field noise heating in ion traps caused by electrode surface adsorbates, *New J. Phys.* **21**, 053043 (2019).
- [28] P. T. Lloyd, V. Walther, and H. Sadeghpour, Correlated many-body noise and emergent $1/f$ behavior, *Phys. Rev. A* **105**, L010402 (2022).
- [29] B. L. Foulon, K. G. Ray, C.-E. Kim, Y. Liu, B. M. Rubenstein, and V. Lordi, $1/\omega$ electric-field noise in surface ion traps from correlated adsorbate dynamics, *Phys. Rev. A* **105**, 013107 (2022).
- [30] P. Dutta and P. Horn, Low-frequency fluctuations in solids: $\frac{1}{f}$ noise, *Rev. Mod. Phys.* **53**, 497 (1981).
- [31] G. Kresse and J. Furthmüller, Efficient iterative schemes for ab initio total-energy calculations using a plane-wave basis set, *Phys. Rev. B* **54**, 11169 (1996).
- [32] G. Kresse and J. Furthmüller, Efficiency of ab-initio total energy calculations for metals and semiconductors using a plane-wave basis set, *Comput. Mater. Sci.* **6**, 15 (1996).
- [33] G. Kresse and D. Joubert, From ultrasoft pseudopotentials to the projector augmented-wave method, *Phys. Rev. B* **59**, 1758 (1999).
- [34] P. E. Blöchl, Projector augmented-wave method, *Phys. Rev. B* **50**, 17953 (1994).
- [35] J. P. Perdew, K. Burke, and M. Ernzerhof, Generalized Gradient Approximation Made Simple, *Phys. Rev. Lett.* **77**, 3865 (1996).
- [36] V. Wang, N. Xu, J.-C. Liu, G. Tang, and W.-T. Geng, VASPKIT: A user-friendly interface facilitating high-throughput computing and analysis using VASP code, *Comput. Phys. Commun.* **267**, 108033 (2021).
- [37] K. T. Chan, J. Neaton, and M. L. Cohen, First-principles study of metal adatom adsorption on graphene, *Phys. Rev. B* **77**, 235430 (2008).
- [38] A. Michaelides, P. Hu, M.-H. Lee, A. Alavi, and D. King, Resolution of an Ancient Surface Science Anomaly: Work Function Change Induced by n Adsorption on W{100}, *Phys. Rev. Lett.* **90**, 246103 (2003).
- [39] K. Momma and F. Izumi, VESTA 3 for three-dimensional visualization of crystal, volumetric and morphology data, *J. Appl. Crystallogr.* **44**, 1272 (2011).
- [40] D. R. Lide, *CRC Handbook of Chemistry and Physics* (CRC, Boca Raton, FL, 2004), Vol. 85.
- [41] S. Machlup, Noise in semiconductors: Spectrum of a two-parameter random signal, *J. Appl. Phys.* **25**, 341 (1954).
- [42] G. Antczak and G. Ehrlich, Jump processes in surface diffusion, *Surf. Sci. Rep.* **62**, 39 (2007).
- [43] C. L. Degen, F. Reinhard, and P. Cappellaro, Quantum sensing, *Rev. Mod. Phys.* **89**, 035002 (2017).
- [44] N. P. de Leon, K. M. Itoh, D. Kim, K. K. Mehta, T. E. Northup, H. Paik, B. Palmer, N. Samarth, S. Sangtawesin, and D. Steuerman, Materials challenges and opportunities for quantum computing hardware, *Science* **372**, eabb2823 (2021).
- [45] F. Hofmann and J. P. Toennies, High-resolution helium atom time-of-flight spectroscopy of low-frequency vibrations of adsorbates, *Chem. Rev.* **96**, 1307 (1996).
- [46] Q. Meng and H.-D. Meyer, MCTDH study on vibrational states of the CO/Cu(100) system, *J. Chem. Phys.* **139**, 164709 (2013).
- [47] D. Goldwater, P. Barker, A. Bassi, and S. Donadi, Quantum Spectrometry for Arbitrary Noise, *Phys. Rev. Lett.* **123**, 230801 (2019).
- [48] A. R. Milne, C. Hempel, L. Li, C. L. Edmunds, H. J. Slatyer, H. Ball, M. R. Hush, and M. J. Biercuk, Quantum Oscillator Noise Spectroscopy via Displaced Cat States, *Phys. Rev. Lett.* **126**, 250506 (2021).
- [49] J. Keller, P.-Y. Hou, K. C. McCormick, D. C. Cole, S. D. Erickson, J. J. Wu, A. C. Wilson, and D. Leibfried, Quantum Harmonic Oscillator Spectrum Analyzers, *Phys. Rev. Lett.* **126**, 250507 (2021).
- [50] I. Talukdar, D. Gorman, N. Daniilidis, P. Schindler, S. Ebadi, H. Kaufmann, T. Zhang, and H. Häffner, Implications of surface noise for the motional coherence of trapped ions, *Phys. Rev. A* **93**, 043415 (2016).
- [51] Z. Liu, L. Chen, J. Li, H. Zhang, C. Li, F. Zhou, S. Su, L. Yan, and M. Feng, Structural phase transition of the ion crystals embedded in an optical lattice, *Phys. Rev. A* **102**, 033116 (2020).
- [52] Y.-Q. Wei, Q. Yuan, L. Chen, T.-H. Cui, J. Li, S.-Q. Dai, F. Zhou, and M. Feng, Time and Frequency Resolution of Alternating Electric Signals via Single-Atom Sensor, *Phys. Rev. Appl.* **19**, 064062 (2023).
- [53] K. Vahala, M. Herrmann, S. Knünz, V. Batteiger, G. Saathoff, T. Hänsch, and T. Udem, A phonon laser, *Nat. Phys.* **5**, 682 (2009).
- [54] I. S. Grudinin, H. Lee, O. Painter, and K. J. Vahala, Phonon Laser Action in a Tunable Two-Level System, *Phys. Rev. Lett.* **104**, 083901 (2010).
- [55] M. Ip, A. Ransford, A. M. Jayich, X. Long, C. Roman, and W. C. Campbell, Phonon Lasing from Optical Frequency Comb Illumination of Trapped Ions, *Phys. Rev. Lett.* **121**, 043201 (2018).
- [56] B. He, L. Yang, and M. Xiao, Dynamical phonon laser in coupled active-passive microresonators, *Phys. Rev. A* **94**, 031802 (2016).
- [57] M. R. Hush, W. Li, S. Genway, I. Lesanovsky, and A. D. Armour, Spin correlations as a probe of quantum synchronization in trapped-ion phonon lasers, *Phys. Rev. A* **91**, 061401 (2015).
- [58] F. Domínguez, I. Arrazola, J. Doménech, J. S. Pedernales, L. Lamata, E. Solano, and D. Rodríguez, A single-ion reservoir as a high-sensitive sensor of electric signals, *Sci. Rep.* **7**, 8336 (2017).
- [59] Z. Liu, Y. Wei, L. Chen, J. Li, S. Dai, F. Zhou, and M. Feng, Phonon-Laser Ultrasensitive Force Sensor, *Phys. Rev. Appl.* **16**, 044007 (2021).
- [60] P. Gartland, S. Berge, and B. Slagsvold, Photoelectric Work Function of a Copper Single Crystal for the (100), (110), (111), and (112) Faces, *Phys. Rev. Lett.* **28**, 738 (1972).